CrossMark

A damage mechanics approach to the simulation of hydraulic fracturing/shearing around a geothermal injection well

Justin Pogacnik [a,*], Derek Elsworth [b], Michael O'Sullivan [a], John O'Sullivan [a]

[a] Department of Engineering Science, University of Auckland, Level 3, 70 Symonds St, Auckland 1142, New Zealand
[b] Department of Energy and Mineral Engineering, Pennsylvania State University, 231 Hosler Building, University Park, PA 16802, USA

A B S T R A C T

Enhanced geothermal energy production requires the stimulation of natural fracture pathways to increase fluid flow within a reservoir while still effectively recovering the heat. During injection/production, reservoir permeability exhibits various degrees of enhancement or degradation with time. These changes are generally attributed to various multiphysics processes that act both during short-term stimulation and during production over the longer term. Important mechanisms of stimulation include tensile failure by hydraulic fracturing or shear failure by hydraulic shearing. A wide range of methods have been used to numerically simulate permeability enhancement in porous and fractured media including models based on damage mechanics, discrete fracture mechanics, critical shear strain criteria, effective stress, and even empirical permeability multipliers. We explore the use of damage mechanics to represent hydraulic fracturing/shearing within the reservoir. The model incorporates an energy release rate micro-crack model in mixed modes (opening – I and shear – II) to simulate damage and permeability enhancement. The model is calibrated against compression tests to determine interrelationships between damage and both deformation and permeability. It is then applied to contrast both isothermal and thermal quenching effects during stimulation of hot reservoirs with cold fluid injection. The results illustrate that when fluid pressures are sub-failure, the damage zone is limited to the near wellbore region. As fluid pressure is increased, near wellbore mode II failure transitions to mode I hydraulic fracturing and rapidly increasing damage. A method of simulating cold water injection induced damage due to both shear and tensile failures is needed in the geothermal industry. This work offers a step forward in that direction.

© 2015 Elsevier Ltd. All rights reserved.

1. Introduction and background

Permeability is one of the most crucial hydrologic parameters and can vary over 16 orders of magnitude [19]. Permeability often determines the feasibility of projects involving geologic processes and their economic potential. This is especially true in geothermal energy production. Enhanced geothermal energy production requires the stimulation of natural fracture pathways to increase fluid flow without creating "short circuits" that allow cold fluid to quickly pass through a system without gaining sufficient heat energy. Changes in permeability are generally attributed to various multiphysics processes that act both during short-term stimulation and during production over the longer term. Important mechanisms of stimulation include tensile failure by hydrofracking or shear failure by hydroshearing; there is a growing interest in the latter as it potentially contributes to a large stimulated volume

of self-propped fractures that is advantageous to heat transfer. In addition, the long term response is modulated by processes of chemical alteration (dissolution and precipitation), thermal and poroelastic deformation of fractures or of the rock matrix, or inelastic failure. All of these processes contribute to the evolution of permeability within the reservoir. A wide range of methods has been used to numerically simulate permeability evolution in porous and fractured media. Models based on damage mechanics, discrete element methods, critical shear strain criteria, cohesive zone finite elements, the eXtended Finite Element Method (XFEM), effective stress, and even empirical permeability multipliers have been proposed.

Clark [9] published perhaps the first paper on hydraulic fracturing (hydrofracking), then termed "pressure parting," which was targeted toward increasing oil well productivity. Hydrofracking is understood to occur when injection pressure exceeds the minimum principal stress. It is characterized by fractures opening in tension and results in the development of highly permeable fracture pathways. An alternative stimulation technique is termed

---

* Corresponding author.
E-mail address: j.pogacnik@auckland.ac.nz (J. Pogacnik).

"hydroshearing." The term was coined to indicate that existing fractures can dilate and slip in shear at lower pressures than are required by hydrofracking [8]. A benefit of this work's mixed mode approach is that both hydroshearing and hydrofracking and the transition between the two stimulation techniques can be simulated with this approach.

A common fracture modeling approach in finite element analyses involves representing a fracture as a discontinuity and using cohesive zone elements to control the failure energy. The concept of a cohesive zone in fracture mechanics can be traced back to the work of Barenblatt [2] and Dugdale [12] and are often referred to as "Plastic Strip Yield Models". The cohesive zone acts as a fracture process zone where a resisting force or traction acts on each crack surface as a function of the displacement jump across the surfaces. Hillerborg et al. [18] were the first to apply a cohesive zone model in finite element analysis to investigate crack formation and growth in concrete. Cohesive zone models have been used to simulate hydraulic fracturing in hydro-mechanical models [7,40,6]. In those works (and traditionally), the crack path was specified *a priori*, so the locations of the cohesive elements were known. However, there are formulations that allow for the dynamic insertion of cohesive elements between any elements of the finite element mesh (e.g., [47]). One of the main difficulties in traditional cohesive zone modeling is overcoming mesh dependencies, as fractures propagate along element edges.

The XFEM allows for discontinuities to cut directly through elements of a mesh [33]. This technique largely overcomes the problems with mesh dependencies in fracture discontinuity techniques. Cohesive zone models have also been applied to the XFEM [32]. The XFEM technique has been used to model the behavior of single fractures in THM modeling by Khoei et al. [25] and for modeling hydraulic fracturing in a poroelastic medium [34]. Recently, Gupta and Duarte [16] have developed a technique using the XFEM in 3D hydraulic fracture simulations allowing for non-planar crack propagation. The main strength of the XFEM is its ability to represent large-scale discontinuities without remeshing. However, in reservoir rock, micro-scale discontinuities exist and can affect permeability and other material behaviors. These defects can perhaps be much smaller than the size of the finite elements.

Damage mechanics is a branch of continuum mechanics that incorporates micro-scale effects into the continuum scale model through the damage variable [10]. Early damage mechanics work was focused on expressing failure in metallic materials. Lemaitre [27] provided an early treatise on the theory and usage of damage mechanics for explaining the behavior of metals under high loads. Mazars and Pijauder-Cabot [31] extended damage mechanics theory for applications related to brittle materials such as concrete and implemented it into finite element simulations. Halm and Dragon [17] developed a thermodynamically consistent, easy-to-use, and anisotropic implementation of damage mechanics into the solid mechanics constitutive theory. Damage mechanics approaches have now been used to study hydraulic fracturing in reservoir rock [48,30]. These papers present a coupled hydro-mechanical framework to test damage-induced permeability enhancement models for application to shale oil plays. A noticeable shortcoming in these approaches (for geothermal) is a lack of consideration of thermal effects as well as non-tensile fracture scenarios such as hydroshearing.

More recent examples of shear stimulation simulations with geothermal applications can be seen in the works of Kelkar et al. [24], Rutqvist et al. [39], and Dempsey et al. [11]. Rutqvist et al. [39] used a simplified Coulomb criterion to determine the volume that would be enhanced by shear failure near an injection site. The initiation criterion was simplified so that it effectively became a maximum principal stress criterion. Their work targeted pre-stimulation behavior and permeability evolution was not taken into account. Kelkar et al. [24] and Dempsey et al. [11] used a Mohr–Coulomb initiation criterion to determine where shear slip occurred near an injection site. Permeability was then altered by either a multiplier [24] or by a sigmoidal function [11], both designed to approximate the measured permeability data obtained by Lee and Cho [26]. These works offer several attractive features, however, the effects of fracture evolution on properties of the solid constitutive theory were not accounted for in these works.

There are also a number of models that use an approach for simulating permeability enhancement by specifying permeability as a function of effective stress [35,36]. In Nathenson [35] stress was simplified to a scalar value and four different effective stress/permeability evolution relationships were tested against geothermal well data. Pogacnik et al. [36] extended Nathenson's "inverse power" relationship to include the full stress tensor. These works do not employ an initiation criterion, so permeability continuously evolved with the stress state. The effective stress relationships of Nathenson [35] can trace their roots back to the cubic law of planar fracture flow popularized by Gangi [14]. While the law theoretically describes flow through a single channel, it often breaks down in complex flow regimes with multiple nonlinear fracture pathways.

In this work, we employ a damage mechanics approach by extending previous work [30,37] to account for a mixed mode fracture criterion that accounts for both shear and tensile failure regimes using microcrack fracture mechanics inside the finite elements. Both shear and tensile failure modes are of interest in Enhanced/Engineered Geothermal Systems (EGS) and a unified model that can account for both modes in a THM simulator has not been previously investigated. THM simulation results of a cold water injection scenario in a uniform 2D medium are shown in the results section. Also, we account for permeability evolution as a result of micromechanical damage that is incurred during loading.

2. Balance equations

2.1. Linear momentum balance for the rock matrix

In this work, inertial forces in the solid rock matrix are ignored. The linear momentum balance (from [4]) is written as:

$$\nabla \cdot \boldsymbol{\sigma} + \mathbf{f} = \mathbf{0} \tag{1}$$

where the vector $\nabla \cdot \boldsymbol{\sigma}$ is the spatial divergence of the Cauchy stress tensor (to be formally defined in the next section) and $\mathbf{f}$ a vector of body forces (both external and density related). Note that bold-face fonts are used to express matrix and vector quantities. The Cauchy stress can be split into two components to represent the effect of pore fluid pressure on the solid matrix [29,19]:

$$\boldsymbol{\sigma} = \boldsymbol{\sigma}'' - \alpha p \mathbf{I} \tag{2}$$

where $\boldsymbol{\sigma}''$ is Biot's effective stress tensor, α is a constant between 0 and 1, p is the pore fluid pressure, and $\mathbf{I}$ is the identity tensor. The effective stress is defined by

$$\boldsymbol{\sigma}'' = \mathbf{C}^D : (\boldsymbol{\varepsilon} - \boldsymbol{\varepsilon}_T) \tag{3}$$

where $\mathbf{C}^D$ is the fourth-order material constitutive tensor (that includes damage), $\boldsymbol{\varepsilon}$ is the strain tensor, ":" represents the double contraction of two tensors, and $\boldsymbol{\varepsilon}_T$ is the thermal strain tensor given by

$$\boldsymbol{\varepsilon}_T = \left(\frac{\beta_s}{3}\right) \Delta T \, \mathbf{I} \tag{4}$$

where β_s is the volumetric coefficient of thermal expansion of the solid and ΔT is the change in temperature from the reference state.

2.2. Mass balance

The pore fluid is assumed to be single phase and consist of fully saturated pure water. The mass balance equation can be written (from [29]):

$$0 = -((1-n)\beta_s + n\beta_w)\frac{\partial T}{\partial t} + \left(\frac{1-n}{K_s} + \frac{n}{K_w}\right)\frac{\partial p}{\partial t}$$
$$+ \nabla \cdot \left\{\frac{\boldsymbol{\kappa}}{\mu_w}[-\nabla p + \rho_w \mathbf{g}]\right\} - Q_p \tag{5}$$

where the subscripts s and w refer to the solid and fluid components respectively, t is time, n is the porosity, K are the bulk moduli, $\boldsymbol{\kappa}$ is the permeability tensor, μ_w is the fluid viscosity, ρ_w is the fluid density, $\mathbf{g}$ is the gravity acceleration vector, and Q_p represents fluid mass flow into the system. The derivation of (5) assumes Darcy flow, linear dependence of porosity, rock density, and fluid density on pressure and temperature.

2.3. Energy balance

Lastly, to couple thermal effects, we introduce the energy balance equation, also from Lewis and Schrefler [29]:

$$0 = (\rho_w C_w + \rho_s C_s)\frac{\partial T}{\partial t} + \rho_w C_w \frac{\boldsymbol{\kappa}}{\mu_w}(-\nabla p + \rho_w \mathbf{g}) \cdot \nabla T - \nabla \cdot \{\chi \cdot \nabla T\} \tag{6}$$

where C represents the specific heat, ρ_s is the density of the solid, and χ is the effective thermal diffusivity of the saturated medium. In (6), fluid viscosity and density were taken to be dependent on temperature only.

We know that parameters such as permeability and Cauchy stress depend upon the deformation state of the material. One possible theoretical framework for capturing this dependency is damage mechanics. The necessary details for this work will be discussed in the following sections.

3. Constitutive equations

3.1. Damage mechanics

Kachanov [22] is credited with the original formulation of damage mechanics. Lemaitre [28] explains that it is useful to view Kachanov's description as a one-dimensional surface damage variable in a system under uniaxial load as seen in Fig. 1. Damage may be interpreted at the microscale as the creation of microsurfaces of discontinuities. At the mesoscale, the number of broken bonds or the pattern of microcavities may be approximated in any plane by the area of the intersections of all the flaws with that plane:
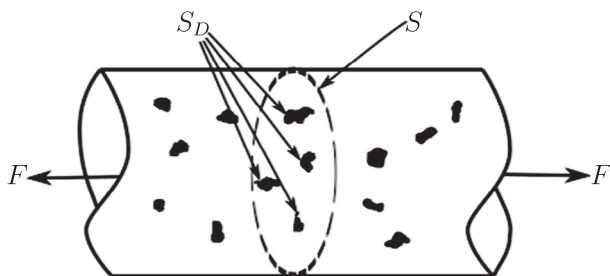
$$D = \frac{S_D}{S} \tag{7}$$

Fig. 1. 1-D damaged bar under uniaxial load (adapted from [28]).

where S is the area of intersection of a plane with a representative volume element and S_D is the effective area of the intersections of all microcracks and cavities that lie in S. In the extremes, if the surface S contains zero microcracks, the damage scalar $D = 0$ and if the surface is entirely composed of microcracks, the damage scalar $D = 1$. A critical isotropic damage value D_c exists that corresponds to total rupture of the solid. That value is reported to typically be between 0.2 and 0.8 in metals based on experimental evidence [27]. In the simplest terms, damage could be taken to reduce the Youngs modulus (E) of the material by a factor:

$$\widetilde{E} = (1-D)E \tag{8}$$

where $\widetilde{E}$ can be viewed as an "effective" Young's modulus.

The first step in applying damage mechanics is to define the damage variable. The damage variable could be defined by a scalar, a second-order tensor, or a fourth-order tensor [10]. In this work, we define damage as a second-order tensor. This allows for either isotropic or anisotropic damage descriptions and is relatively easy to implement and computationally inexpensive. However, in all the example problems presented here, we have utilized isotropic damage, so each component of the damage tensor was taken to be equal. The damage tensor is defined by

$$\mathbf{D} = \sum_k d_k \mathbf{n}_k \otimes \mathbf{n}_k \tag{9}$$

where d_k is a dimensionless scalar function between 0 and 1 proportional to the theoretical microcrack length in a representative volume element and $\mathbf{n}_k$ are unit normal vectors that characterize the direction of the microcrack [30]. If an element is completely intact without damage, $d_k = 0$; in the completely damaged case, $d_k = 1$. The completely damaged case would correspond to material failure and the inability to transmit stress. In a similar fashion to Lu et al. [30], the damage scalar d_k is defined as

$$d_k = D_{\max}\frac{a_k^2 - a_0^2}{a_0^2} \tag{10}$$

where a_k is the crack length of the kth microcrack in an element and a_0 is the original crack length. As this work is limited to 2D and (10) is only valid for that case, however, Lu et al. [30] also present the 3D equivalent. We assume that a single microcrack exists in the element that it is favorably oriented to the principal stress directions to result in a maximum energy release rate (to be defined in the next section). $D_{\max}$ is the maximum damage value that results in complete rupture that could be determined based on experimental evidence. Its value is bounded by "1". In order to bound the maximum value of d_k to be $D_{\max}$, we also set a maximum crack length in this work and did not allow damage or crack length to increase past that point. This ensures that the damage evolution can empirically match experimental data for bulk behaviors such as stress–strain and permeability–strain, but may be incorrect regarding absolute magnitudes of microcrack length. However, the authors lack experimental microcrack data, so these crack lengths are best viewed as estimates. Ideally, a critical crack length would be that which results in element failure and $d_k = D_{\max}$. Solving Eq. (10) for $d_k = D_{\max}$ gives $a_{\max} = a_0\sqrt{2}$. Together with a constitutive model to determine the effect damage has on the stress–strain response, linear elastic fracture mechanics can be used to compute the evolution of the microcrack length a_k.

3.2. Solid mechanics constitutive model

Damage is the process of the initiation and growth of microcracks and cavities [42]. At the micro-scale, these phenomena are discontinuous. Damage could be considered as a deterioration process similar to irreversible strain [3]. The damage variable is writ-

ten in terms of stress or strain and can be used in solid mechanics analyses to predict the initiation and evolution of microcracks. These cracks can affect a variety of parameters including, but not limited to, material stiffness and permeability.

A strain energy density function serves as the starting point of constitutive model development and describes the work done by stresses to deform a body from the initial configuration to the deformed configuration. The strain energy density function can be expressed in terms of damage as [17]:

$$\Psi(\boldsymbol{\varepsilon}, \mathbf{D}) = \frac{1}{2}\lambda\,\mathrm{tr}(\boldsymbol{\varepsilon})^2 + \eta\boldsymbol{\varepsilon} : \boldsymbol{\varepsilon} + F\boldsymbol{\varepsilon} : \mathbf{D} + A\mathrm{tr}(\boldsymbol{\varepsilon})\boldsymbol{\varepsilon} : \mathbf{D} + 2B(\boldsymbol{\varepsilon} : \boldsymbol{\varepsilon}) : \mathbf{D} \tag{11}$$

where $\mathrm{tr}(\cdot)$ denotes the trace of a tensor, λ and η are the Lamé parameters, F is a constant governing residual damage effects (similar to permanent deformation), A and B are supplementary damage constants related to moduli degradation and $\mathbf{D}$ is the second order damage tensor defined in the previous section. Taking the first derivative of the strain energy density with respect to strain yields the Cauchy stress tensor:

$$\boldsymbol{\sigma} = \frac{\partial \Psi}{\partial \boldsymbol{\varepsilon}} = \lambda\,\mathrm{tr}(\boldsymbol{\varepsilon})\mathbf{I} + 2\eta\boldsymbol{\varepsilon} + F\mathbf{D} + A[\mathrm{tr}(\boldsymbol{\varepsilon}\mathbf{D})\mathbf{I} + \mathrm{tr}(\boldsymbol{\varepsilon})\mathbf{D}] + 2B(\boldsymbol{\varepsilon}\mathbf{D} + \mathbf{D}\boldsymbol{\varepsilon}) \tag{12}$$

Application of an additional derivative with respect to strain gives the fourth-order damage elasticity tensor show in Eq. (3). In indicial notation:

$$\begin{aligned} C^D_{IJKL} &= \frac{\partial \sigma_{IJ}}{\partial \varepsilon_{KL}} = \frac{\partial^2 \Psi}{\partial \varepsilon_{IJ}\partial \varepsilon_{KL}} \\ &= \lambda\delta_{IJ}\delta_{KL} + \eta\big(\delta_{IK}\delta_{JL} + \delta_{IL}\delta_{JK}\big) + A\big(\delta_{IJ}D_{KL} + D_{IJ}\delta_{KL}\big) \\ &\quad + B\big(\delta_{IK}D_{JL} + \delta_{IL}D_{JK} + D_{IK}\delta_{JL} + D_{IL}\delta_{JK}\big) \end{aligned} \tag{13}$$

This simple formulation was proven to be thermodynamically consistent by Halm and Dragon [17] and is powerful as it is easy to implement in any finite element code in the same way that any nonlinear elastic material model may be implemented. The inclusion of damage in the solid constitutive model allows for the simulation of nonlinear stress strain behavior that is associated with damage evolution in the material and ultimately the simulation of material failure as well. There are notable drawbacks to this approach, predominantly, the exclusion of plastic constitutive behavior. Materials that undergo plastic deformation do behave differently under increments of shear stress than do elastic materials [5]. Therefore, this approach would be expected to have a reduced shear stress localization effect. However, for small strains in brittle materials, the approach outlined in this work is reasonable. The interested reader is pointed toward the works of Voyiadjis and Kattan [42] for implementation of damage mechanics with plastic constitutive models.

The evolution of the damage tensor $\mathbf{D}$ can be controlled through almost any function of stress and strain [48]. de Borst et al. [10] present a strain energy measure more appropriate for metals, while Mazars and Pijauder-Cabot [31] developed a strain dependent formulation for brittle materials such as rock or concrete. Stress-based plasticity yield conditions can also be used such as the Drucker-Prager or Mohr–Coulomb conditions. In this work we adopt a similar approach to Lu et al. [30] based on critical fracture mechanics quantities. The next section will outline the fracture mechanics used to determine damage evolution in this work.

4. Fracture mechanics

Inglis [20] first derived the analytical stress concentrations around an elliptical flaw and Griffith [15] invoked the first law of thermodynamics to formulate a fracture theory based on an energy balance. Consider Fig. 2 which shows a section of an infinite plate subject to a biaxial state of stress with a flaw of length $2a$ oriented at angle α. In the figure, σ_2 is the principal stress with the lower magnitude, regardless of sign (+/− for tension/compression in standard engineering notation). In 2D, there are two types of loading that the crack can experience: (1) Mode I, which is applied normal to the crack, acts to open the crack and (2) Mode II, which corresponds to in-plane shear loading and slides one crack surface with respect to the other. In 3D, Mode III also exists, which corresponds to out-of-plane shear loading. The concentration of stresses near the crack tip results in a stress intensity factor, termed K_m where m refers to the mode of loading present. Therefore, a stress intensity factor exists for all loading modes, i.e., $K_I, K_{II},$ and K_{III}. Brittle materials have material parameters called the critical stress intensity factors that are associated with material failure. They are denoted $K_{IC}, K_{IIC},$ and K_{IIIC}. In a brittle material subject to loading in a single plane, failure occurs when $K_m = K_{mC}$.

A useful example is the case where $\alpha = 0°$ and $\sigma_1 = 0$ which corresponds to pure Mode I loading. The Mode I stress intensity can be expressed as:

$$K_{I(0)} = \sigma_2\sqrt{\pi a} \tag{14}$$

For the biaxial case in Fig. 2, the Mode I and II stress intensity factors can be determined from Anderson [1] or Eftis and Subramonian [13]:

$$K_I = K_{I(0)}\Big(\cos^2\alpha + B\sin^2\alpha\Big) \tag{15}$$

$$K_{II} = K_{1(0)}(\sin\alpha\cos\alpha)(1-B) \tag{16}$$

where

$$B = \frac{\sigma_1}{\sigma_2} \tag{17}$$

The relations given in (15)–(17) are valid for biaxial compression, tension, or mixed loading scenarios. However, it should be noted that a negative K_I value indicates that the crack faces pass through each other. Therefore, the theoretical minimum for K_I is 0.

As stated earlier, Irwin developed an energy release rate failure theory based on Griffith's work [21]. The energy release rate is a measure of the energy available for crack extension. It shows that the stress intensity factor values for each mode are additive Anderson [1]:
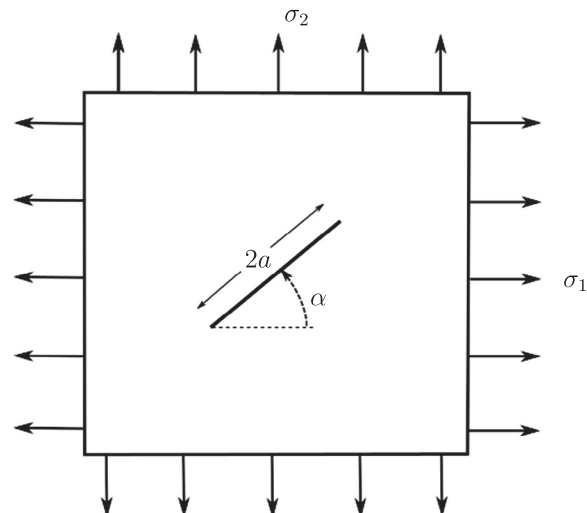

Fig. 2. Cracked plate subject to a biaxial stress state (adapted from [1,13]).

$$\mathcal{G} = \frac{K_I^2}{E'} + \frac{K_{II}^2}{E'} + \frac{K_{III}^2}{2\eta} \qquad (18)$$

where the energy release rate is expressed as $\mathcal{G}$ in homage to Alan Griffith and

$$E' = \frac{E}{1 - \nu^2} \qquad (19)$$

for 2D plane strain and 3D analyses where E is Young's modulus and ν is Poisson's ratio. Similarly to the stress intensity factor, a critical energy release rate $\mathcal{G}_C$ exists that is a material property and results in crack propagation.

5. Permeability enhancement

There is some data in the literature that seeks to characterize permeability as a function of strain, based on experiments. Most of that work is related to the "cubic law" and flow through single fractures [14,44]. There are very few experimental studies that characterize bulk permeability as a function of bulk deformation and most of them are limited to sandstone samples [41,43,46,48]. Those works report permeability values with some variability, e.g., the maximum permeability reported is of the order of 1e−16, 1e−18, 1e−17, and 1e−13 m^2, respectively. For this study, model calibration was based on the normalized permeability–strain curves as shown in Fig. 4. The value of permeability was then scaled to be realistic for a representative geothermal rock. As a starting point for this work, we chose to cast permeability as a function of damage, instead of stress or strain. This enabled a consistent permeability evolution calculation to be performed regardless of the damage evolution criterion used. The permeability function used in this work was [37]:

$$\boldsymbol{\kappa}(\mathbf{D}) = \boldsymbol{\kappa}_0 + \boldsymbol{\kappa}_1(\mathbf{D}) - \boldsymbol{\kappa}_2(\mathbf{D}) \qquad (20)$$

where $\boldsymbol{\kappa}_0$ is the initial (potentially anisotropic) diagonal permeability tensor with individual components κ_0^x, κ_0^y, and κ_0^z. The diagonal matrices $\boldsymbol{\kappa}_1$ and $\boldsymbol{\kappa}_2$ are composed of sigmoidal functions designed to capture permeability changes with damage qualitatively similar to the expected enhancement behavior [37,41,43,46,48] and defined as:

$$\kappa_1^i = \frac{\kappa_{\max} - \kappa_0^i}{1 + exp\left[-\nu_1\left(D^i - D_1\right)\right]} \qquad (21)$$

$$\kappa_2^i = \frac{\kappa_{\max} - \kappa_f}{1 + exp\left[-\nu_2\left(D^i - D_2\right)\right]} \qquad (22)$$

where the superscript $i = x, y$, or z (11, 22 or 33 components of the matrices). Therefore, damage could be anisotropic. However, in this work, we assumed isotropic permeability. The other parameters are all curve fit parameters adjusted based on available experimental data. $\kappa_{\max}, \kappa_0$, and κ_f define the maximum, initial, and final permeability values for each direction; $\nu_{1,2}$ are parameters that adjust the slope of the permeability as a function of damage curve; and $D_{1,2}$ adjust the critical damage values that result in permeability evolution. The results of using this model to match permeability/strain laboratory data can be seen in Fig. 4.

6. Solution strategy

The governing differential equations of (1)–(6) were solved using the finite element method. The details of the discretization technique used can be seen in Pogacnik et al. [38] or Lewis and Schrefler [29]. Application of the finite element method gives rise to the following global system of equations for solution:

$$\mathbf{Ku} - \mathbf{Qp} - \mathbf{K}_{uT}\mathbf{T} = \mathbf{f}_u \qquad (23)$$

$$\mathbf{Hp} + \mathbf{S}\frac{\partial \mathbf{p}}{\partial t} + \mathbf{R}\frac{\partial \mathbf{T}}{\partial t} = \mathbf{f}_p \qquad (24)$$

$$\mathbf{K}_T\mathbf{T} + \mathbf{C}_T\frac{\partial \mathbf{T}}{\partial t} = \mathbf{f}_T \qquad (25)$$

where the unknown primary variable vectors are $\mathbf{u}$ = displacement, $\mathbf{p}$ = pore fluid pressure and $\mathbf{T}$ = temperature. The interested reader is directed toward Pogacnik et al. [38] for the details of the matrices and right hand side forcing vectors.

Eqs. (23)–(25) were solved using what is often called an "iterative split operator algorithm" (ISO) or "sequential iterative approach" (SIA) from Yeh and Tripathi [45] or Kanney et al. [23] by first solving for $\mathbf{p}$ and $\mathbf{T}$ simultaneously, then using those results to solve for $\mathbf{u}$, then iterating until convergence before marching on in time. Algorithm 1 gives pseudocode for the SIA algorithm used in this work.

Algorithm 1. Pseudocode for sequential iterative approach (SIA)

---
1 · Define geometry and grid
2 · Define initial material properties
3 · Setup initial conditions
4 for t in timesteps **do**
5 | · Setup boundary conditions
6 | **while** Global Error > 10^{-10} **do**
7 | | · Solve TH problem by Eq. (27)
8 | | · Solve M problem by Eq. (23) using $\mathbf{p}, \mathbf{T}$
9 | | **for** e in elements **do**
10 | | | · Compute $\mathcal{G}$ in current element by (18)
11 | | | **if** $\mathcal{G} > \mathcal{G}_C$ **then**
12 | | | | · Update crack length (a_k) so that $\mathcal{G} = \mathcal{G}_C$
13 | | | | · Update damage using (10)
14 | | | | **if** $a_k \geqslant a_{\max}$ **then**
15 | | | | | · Element rupture!
16 | | | | | · $d_k = D_{\max}$
17 | | | | **end**
18 | | | | · Update permeability using (20)–(22)
19 | | | **end**
20 | | **end**
21 | **end**
22 end

After the discretization of the geometry and setup of the initial material properties and conditions, time stepping can begin. Boundary conditions were then set up as they could be time dependent. We chose a global convergence criterion of the maximum L_2 norm in the change of the primary variable vectors $\mathbf{u}, \mathbf{p}$, and $\mathbf{T}$ to be less than a tolerance (1.0×10^{-10}). That is,

$$\|\mathbf{x}\|_2 = \sqrt{(\mathbf{x}_i - \mathbf{x}_{i-1})^2} < 1.0 \times 10^{-10} \qquad (26)$$

where $\mathbf{x} = \mathbf{u}, \mathbf{p},$ and, $\mathbf{T}$ and i is the iteration counter of the global convergence loop. To solve the TH problem, Eqs. (24) and (25) can be recast in the following matrix system of equations:

$$\begin{bmatrix} \mathbf{H} & \mathbf{0} \\ \mathbf{0} & \mathbf{K}_T \end{bmatrix} \begin{bmatrix} \mathbf{p} \\ \mathbf{T} \end{bmatrix} + \begin{bmatrix} \mathbf{S} & \mathbf{R} \\ \mathbf{0} & \mathbf{C}_T \end{bmatrix} \frac{d}{dt} \begin{bmatrix} \mathbf{p} \\ \mathbf{T} \end{bmatrix} = \begin{bmatrix} \mathbf{f}_p \\ \mathbf{f}_T \end{bmatrix} \qquad (27)$$

that can then be solved by a single step finite difference operator as in Lewis and Schrefler [29] and the Newton–Raphson (NR) iteration procedure. During the NR iteration step, we enforced a tolerance of 1.0×10^{-16} in the L_2 norm of the change in the unknown vectors. After solving (27), the resulting $\mathbf{p}$ and $\mathbf{T}$ vectors can be substituted

into (23) to solve for the solid displacements. The stiffness matrix **K** was set up in the usual way, i.e.,

$$\mathbf{K} = \int_{\Omega_e} \mathbf{B}\mathbf{C}_D\mathbf{B}\, d\Omega_e \tag{28}$$

where **B** are ordinary finite element matrices containing the shape function derivatives (see [29]), Ω_e is the domain of the current element e, and $\mathbf{C}_D$ is the stiffness matrix created by collapsing the indices of the fourth-order elasticity tensor from Eq. (13) due to symmetries. Recall that the elasticity tensor is dependent upon the current state of damage in the material. Since the introduction of damage results in a material nonlinearity, the NR iteration procedure was also performed during the solution of (23) with the same tolerance of 1.0×10^{-16} enforced.

After the solid mechanics calculation, the damage was updated for subsequent global iterations at the current time step. The first step to updating the damage variable was to compute the stress state at the center of each element. The value of Griffith's energy release rate $\mathcal{G}$ was evaluated for each element by Eq. (18). Recall that $\mathcal{G}$ is dependent upon the orientation of the critical micro crack in the element. We tested crack orientations of $\alpha = 0$–$180°$ in $1°$ increments and assumed that a crack existed with the orientation α that resulted in the highest $\mathcal{G}$ value. If $\mathcal{G}$ was higher than the critical energy release rate for the material $\mathcal{G}_C$, then crack growth occurred. The equilibrium crack length a_k for the current stress state results in $\mathcal{G} = \mathcal{G}_C$ [30]. We iterated on crack growth increments until a final crack length a_k was found that resulted in $\mathcal{G} = \mathcal{G}_C$. The scalar damage value d_k was then updated by Eq. (10). Element rupture occurs when $a_k > a_{\max}$ and results in $d_k = D_{\max}$. The damage value then was used to update the permeability by Eqs. (20)–(22). The computation then returned to the beginning of the current time step to recalculate all the primary variables unknown vectors (**p**, **T**, and **u**). This again was followed by crack length and damage updates until the change in the global iteration norm was below the specified tolerance.

7. Modeling

7.1. Model calibration

It is first necessary to calibrate the numerical model with some known data. While there is little laboratory data that studies the relationship between the stress–strain state and permeability, some work has been performed on brittle reservoir sedimentary rocks. Examples of these exercises can be seen in Tang et al. [41], Wang and Park [43], Zhang et al. [46], Zhou et al. [48]. The calibration method used here was identical to the method performed in Pogacnik et al. [37], however that work did not utilize a mixed mode initiation criterion, but a critical strain energy initiation criterion.

For calibration of the stress–strain and permeability–strain responses, we used compression test data from Tang et al. [41], Wang and Park [43], Zhang et al. [46], Zhou et al. [48]. Fig. 3 displays the stress–strain result of the model compared to the experimental data. In this analysis, the parameter F of Eq. (12) was set to 0. This is valid assuming that no unloading or cyclic loading is present. The parameters A and B were chosen to be equal to $-\lambda/2$ and $-\eta/2$ respectively so that in the case of maximum damage ($\mathbf{D} = \mathbf{I}$), the Cauchy stress calculated by (12) returns a zero stress state and thus, a zero stiffness analogous to Eq. (8). Young's modulus E was set to be 17.0 GPa and Poisson's ratio ν was set to be 0.2. A complete list of all the material properties used in this study is presented in the next section in Table 3. Fig. 4 displays the permeability–strain result of the model compared to experimental data. The permeability enhancement-related material properties used in Eqs. (21) and (22) are presented in Table 1. As noted in
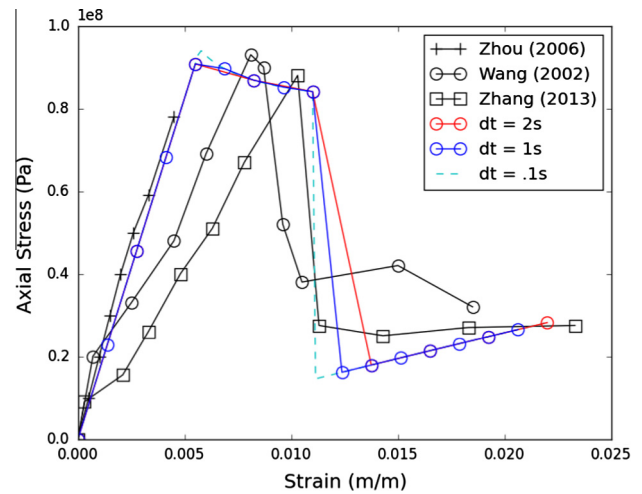
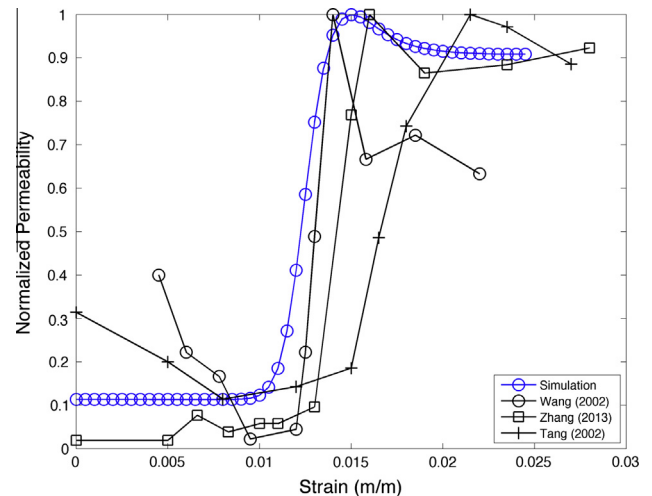**Fig. 3.** Stress–strain response for sandstone samples from data in the literature and calibrated response of this model.

Fig. 4. Permeability–strain response for sandstone samples from data in the literature and calibrated response of this model.

Table 1
Material parameters for permeability enhancement.

Parameter	Value
κ_0	1.0×10^{-15} m^2
$\kappa_{\max}$	5.0×10^{-14} m^2
κ_f	4.0×10^{-14} m^2
v_1	100
v_2	100
D_1	0.50
D_2	0.85

the previous section, the available experimental data for permeability had very large differences, even within sandstone samples. Therefore, the permeability values were normalized for calibration. Table 2 displays the minimum and maximum reported permeabilities for sandstone samples from each reference.

7.2. Simulation set-up

Two different finite element geometries were tested in this work. The first was a 2-D confined compression cylinder based on the geometry used for confined compression experiments by

Table 2
Permeability values from experimental works.

Reference	κ_{min} (m^2)	κ_{max} (m^2)
Tang et al. [41]	5.0×10^{-17}	4.0×10^{-16}
Wang and Park [43]	1.5×10^{-20}	3.1×10^{-18}
Zhou et al. [48]	1.0×10^{-17}	1.0×10^{-13}
Zhang et al. [46]	1.0×10^{-18}	7.0×10^{-17}

Wang and Park [43]. The second geometry was used to represent a single geothermal well injection scenario. Figs. 5 and 6 display the geometry and boundary conditions for the confined compression test simulation and single well injection scenario respectively. The material properties used in this work are presented in Table 3.

The confined compression test was set up to be as close as possible to the experiments by Wang and Park [43]. The top surface was loaded at a fixed vertical displacement rate $\dot{u}_y = -0.11$ mm/s and fixed against displacement in the horizontal direction. The bottom surface was fixed against displacement in both the horizontal and vertical directions. The specimen was subjected to a compressive horizontal confining stress $\sigma_H = 5.0$ MPa. The initial pore fluid pressure in the entire domain was set to 4.8 MPa and the top pressure (P_t) was fixed at that value. The bottom pressure (P_b) was set to 3.3 MPa giving $\Delta P = 1.5$ MPa in the isothermal domain. The entire simulation time was 16 s with time steps ranging from 0.1 to 2 s.

In the injection scenario, multiple *in situ* stress and fluid pressure states with different injection pressures were tested. The initial stress, pore fluid pressure, and temperature conditions were all meant to be representative of an area around 3 km depth in a geothermal reservoir. In all cases, the bottom surface was fixed from normal displacement (roller BC) and the center node was pinned from horizontal displacement. Horizontal tractions were placed on the left and right surfaces and a vertical traction was placed on the top surface. The pore fluid pressure and temperature were specified throughout the domain initially. The center well bore was subjected to subsequent over pressurization of pure water (as a function of time) both at the initial temperature and at a lower temperature (isothermal or cold water injection scenarios, respectively). Initially, we tested the isothermal case,
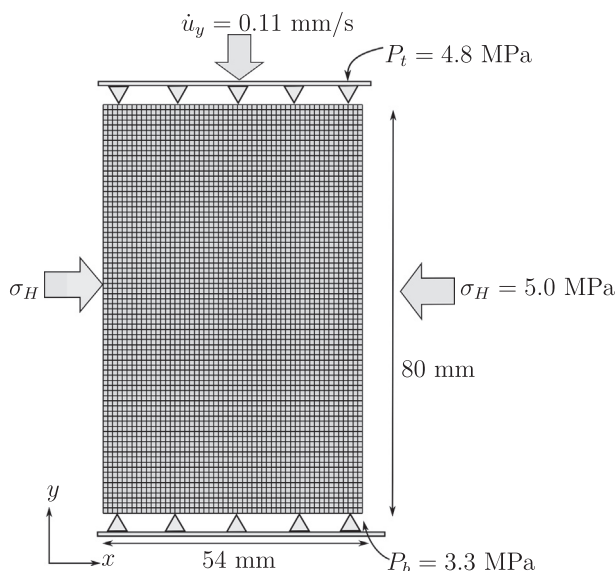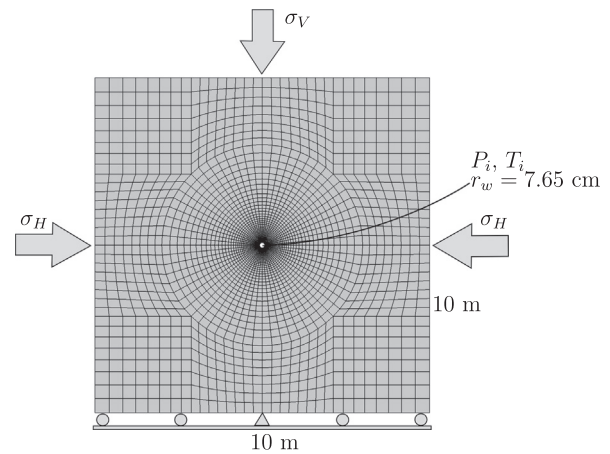

Fig. 6. Geometry for the single well injection scenario simulations.

Table 3
Values of material properties used in this study.

Parameter	Symbol	Value	Units
Rock density	ρ_s	2600.0	kg/m^3
Young's modulus	E	17×10^9	Pa
Poisson's ratio	v	0.20	–
Water bulk modulus	K_w	3.3×10^9	Pa
Rock coefficient of thermal expansion	β_s	1.7×10^{-5}	1/°C
Rock specific heat	C_s	840.0	J/kg °C
Water specific heat	C_w	4187.0	J/kg °C
Critical energy release rate	$\mathcal{G}_c$	4200.0	Pa m
Maximum damage	D_{max}	0.92	–

with different hydrostatic pore fluid pressures to determine what fluid pressure values result in a transition from mode II damage around the well bore to mode I induced damage. Subsequent simulations were designed to determine conditions for fracture propagation and damage states near the well bore due to fluid injection.

8. Results and discussion

8.1. Confined compression test

In the confined compression test simulation, the medium was taken to be uniform and isotropic with no initial damage distribution. While this is not realistic of fractured reservoir rock, it does allow for the calibration of the material model based on the data at hand. The engineering stress strain curve was plotted in Fig. 3 in the previous section and shows a reasonable fit with the experimental data. The figure shows an initial elastic portion, followed by a section of micro crack growth that is similar to a traditional "yield" portion of a stress–strain diagram. The parameter $\mathcal{G}_c$ was calibrated to match the initial "yield" stress portion from these data. When element crack length $a_k = a_{max}$, then the elements were considered to have ruptured and d_k was set to equal D_{max}. This corresponds to a sharp decline in stress when strain is greater than about 0.012 (m/m). The value of D_{max} determines the post failure stiffness of the specimen. We chose 0.92 to achieve the stress values seen at high strains in the experimental data.

To test for time step dependence, time steps of 2 s, 1 s, and 0.1 s were tested. The figure shows that the stress–strain results are the same for each time step size, but the time discretization causes changes in material behavior to be resolved slightly differently (such as the transition that occurs when $a_k \geqslant a_{max}$). However, at coincident times the results for each case were the same (i.e., $t = 2, 4, 6, 8$ s). Fig. 7 shows the damage state of the confined
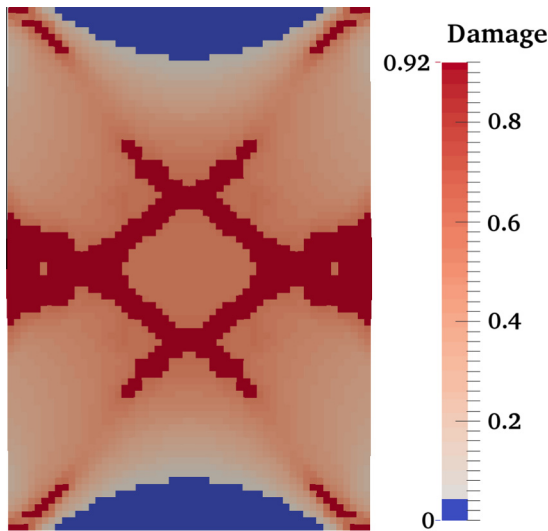

Fig. 5. Geometry of confined compression simulation based on work of Wang and Park [43].

Fig. 7. Damage state of CCT simulation at $t = 8$ s.

compression test at the point of specimen failure ($t = 8$ s). Notice the well-known 45° conjugate shear planes forming in the specimen at failure.

Matching the permeability–strain plots proved to be more difficult than stress–strain behavior. This is probably due to the fact that Eqs. (20)–(22) only express permeability as a function of damage, when it is in fact a complex function of a number of multiphysics phenomena. From Fig. 4, we see that the significant permeability enhancement occurs at large strains (high damage) that is near the failure point of the material. From Eqs. (21) and (22): κ_{max} determines the maximum permeability reached in the simulation; κ_f determines the final enhanced permeability at large strains; and the parameters $D_{1,2}$ adjust the damage values where transitions occur in the permeability behavior. Therefore, increasing D_1 would result in permeability increasing at a larger strain/damage value, while changing D_2 would result in changing the strain/damage value at which permeability settles into its final value. This is an entirely empirical relationship designed to match laboratory behavior. A better relationship is needed and this is the subject of an active field of research.

8.2. Well bore injection scenario

This section presents the results for the various well bore injection scenarios tested in this work. The first case is a damage free isothermal case with equal horizontal and vertical principal stress. The second case includes isothermal and cold water injection scenarios with damage for the same equal principal stresses. The final test case presents results for a hydrofracking simulation with cold
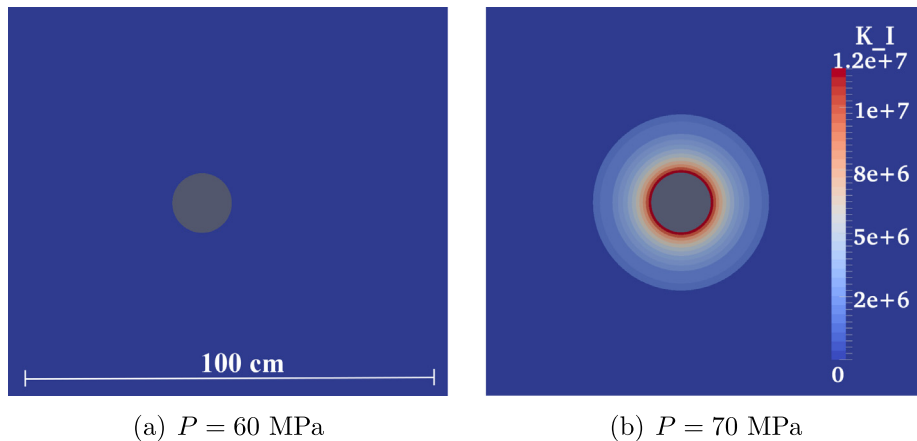

(a) $P = 60$ MPa

(b) $P = 70$ MPa

Fig. 8. Results for mode I stress intensity factor near a well bore in a domain with equivalent biaxial compressive stresses of 70 MPa and pore fluid pressure of (a) 60 MPa and (b) 70 MPa.
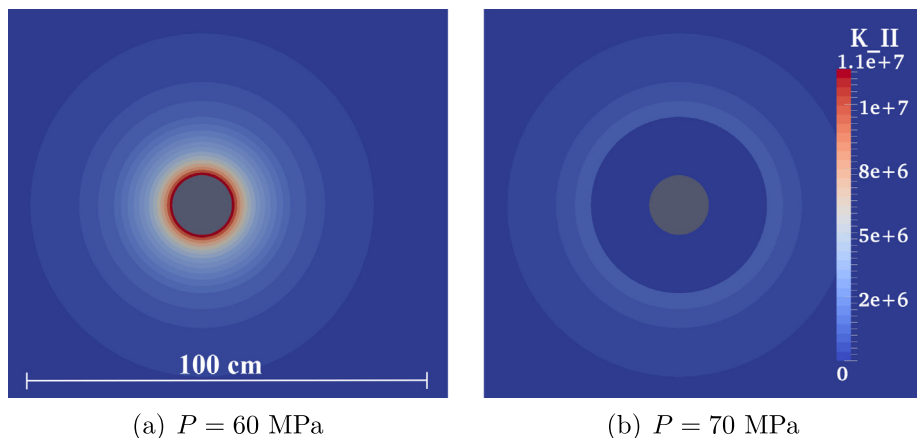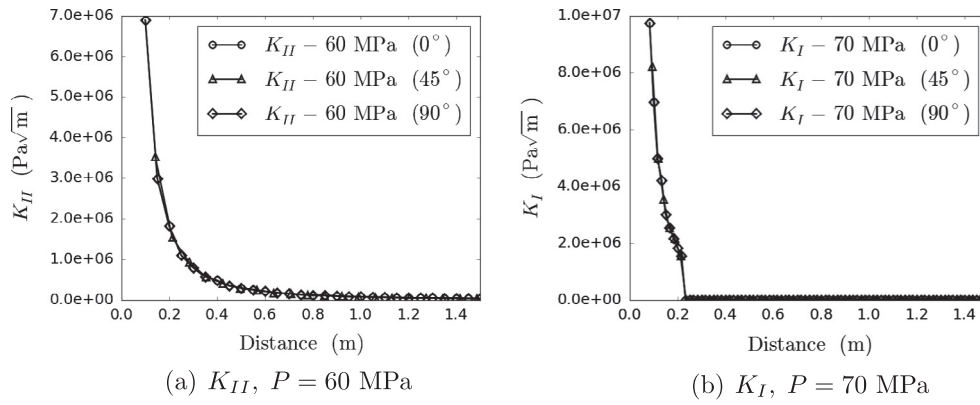

(a) $P = 60$ MPa

(b) $P = 70$ MPa

Fig. 9. Results for mode II stress intensity factor near a well bore in a domain with equivalent biaxial compressive stresses of 70 MPa and pore fluid pressure of (a) 60 MPa and (b) 70 MPa.

(a) K_{II}, $P = 60$ MPa   (b) K_I, $P = 70$ MPa

Fig. 10. Plot of K_{II} from Fig. 9(a) and K_I from Fig. 8(b) at 0°, 45°, and 90°.
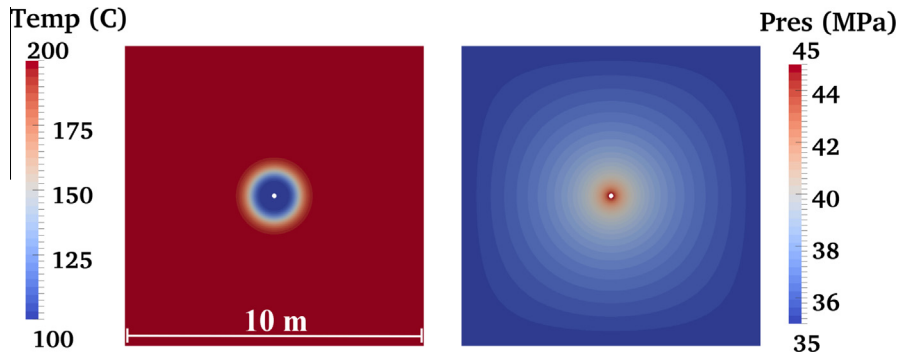

Fig. 11. The temperature response (left) and pressure response (right) after 1000 s of cold water injection in a domain with principal stresses of $\sigma_H = \sigma_V = 70$ MPa.
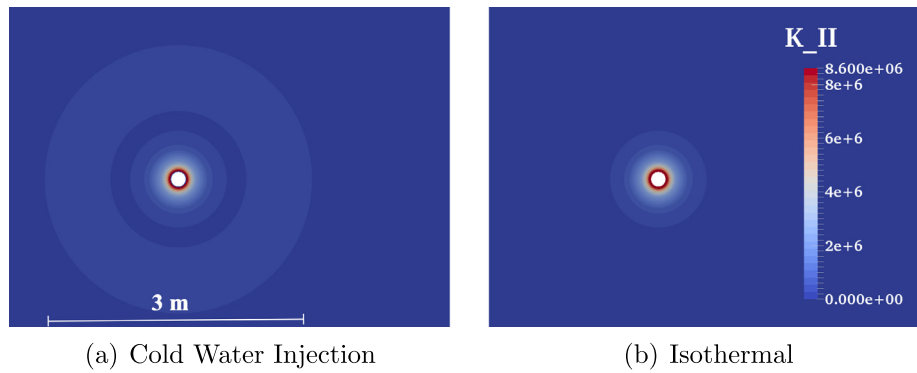

(a) Cold Water Injection   (b) Isothermal

Fig. 12. The mode II stress intensity response near an injection well for a (a) cold water injection scenario and (b) an isothermal injection scenario, each with 70 MPa horizontal and vertical principal stresses applied in a medium subject to an initial pore fluid pressure of 35 MPa and an injection pressure of 45 MPa.
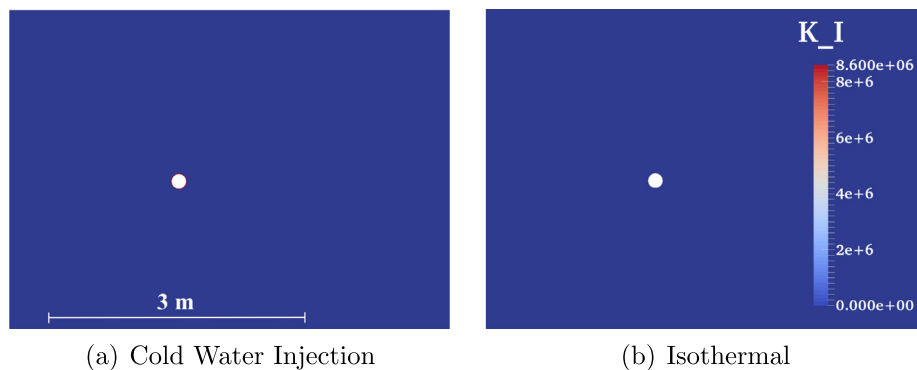

(a) Cold Water Injection   (b) Isothermal

Fig. 13. The mode I stress intensity response for the simulation presented in Figs. 11 and 12.

(a) Cold Water Injection   (b) Isothermal
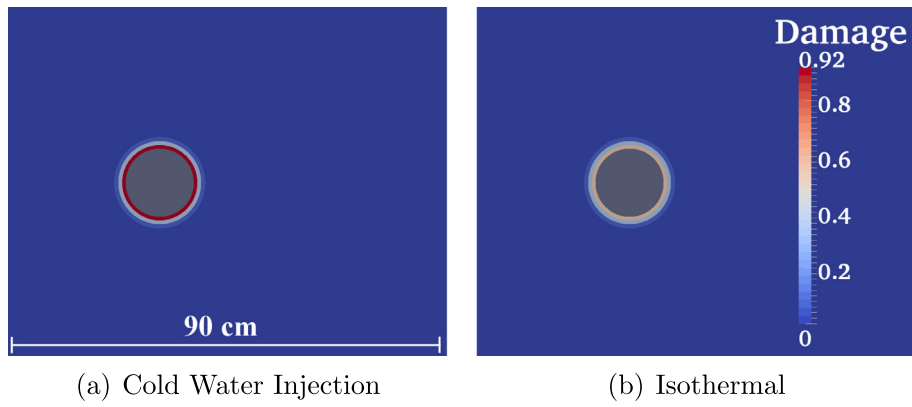
Fig. 14. Isotropic damage around an injection well for the scenarios presented in Figs. 11–13.

(a) t = 100 s   (b) t = 300 s   (c) t = 500 s
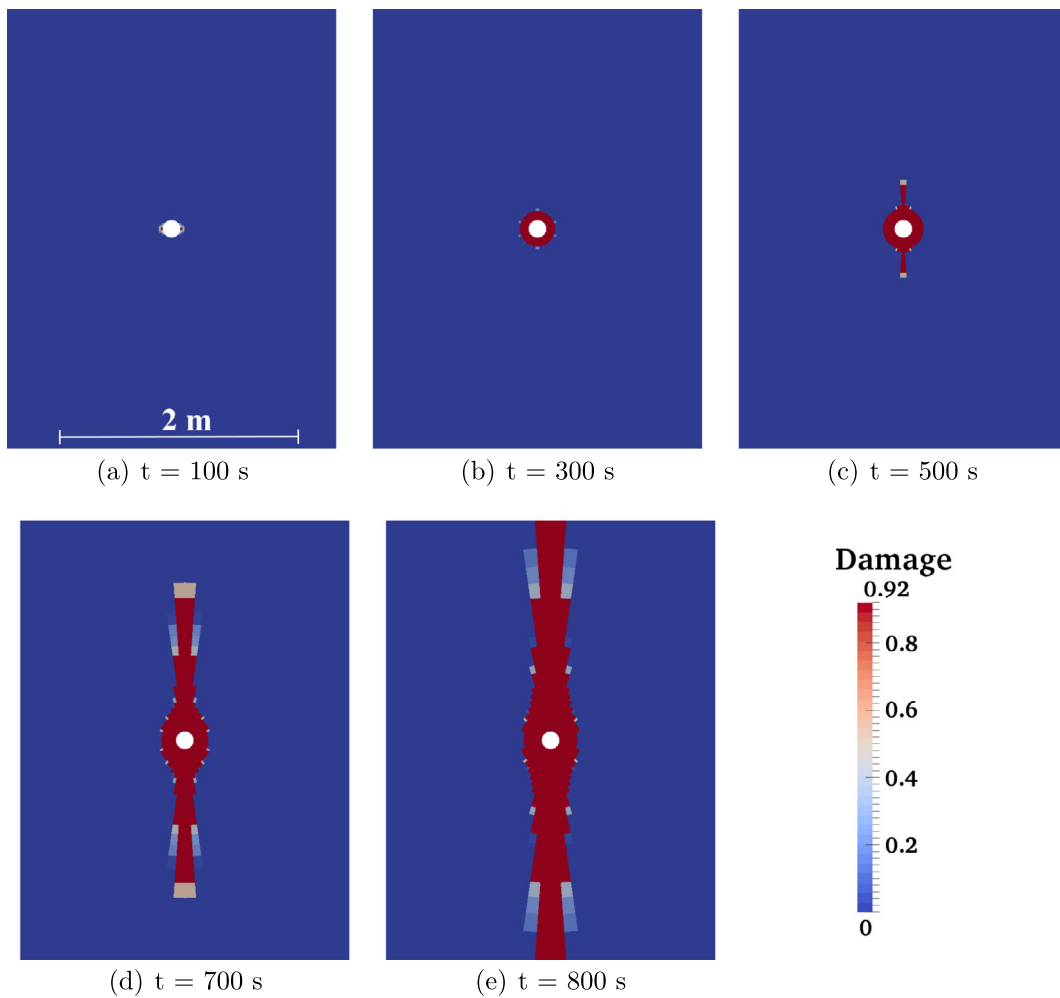
(d) t = 700 s   (e) t = 800 s

Fig. 15. Isotropic damage in near a well bore subject to $\sigma_H = 35$ MPa and $\sigma_V = 70$ MPa with an initial pore fluid pressure of 20 MPa subject to the injection of 100 °C water at 110 MPa.

water injection and unequal horizontal and vertical principal stresses.

8.2.1. Damage free (elastic) case

Fig. 8 displays the mode I stress intensity in the area around the well bore for a case where $\sigma_H = \sigma_V = 70$ MPa and the pore fluid pressure is fixed at 60 MPa in (a) and 70 MPa in (b). Fig. 9 displays the mode II stress intensity factor around well bores in the same stress/pressure state as Fig. 8. Fig. 10 displays the K_{II} result from Figure (a) and the K_I result from figure (b) at $0°, 45°$, and $90°$ from the well bore. This highlights that the problems are radially symmetric, however a 1-D radial model would not be adequate to cap-

(a) t = 100 s   (b) t = 300 s   (c) t = 500 s
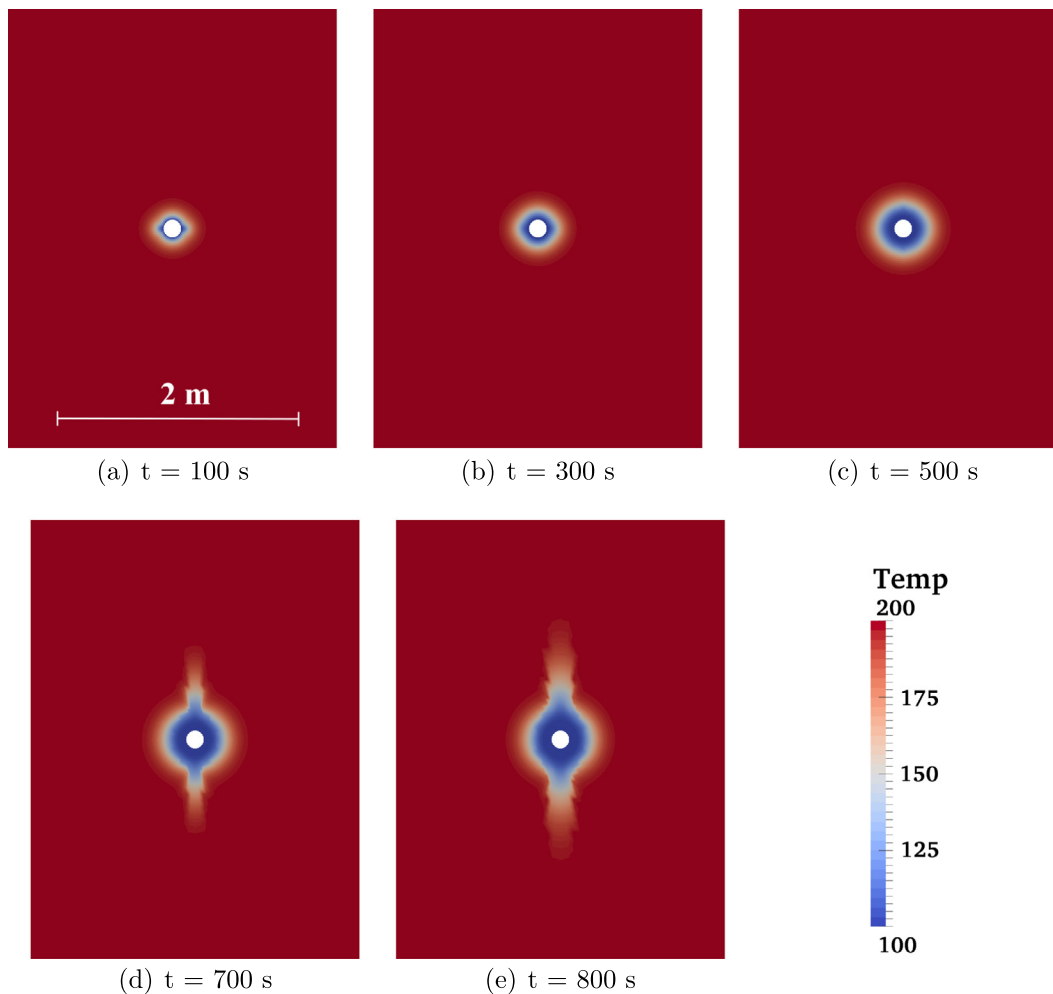
(d) t = 700 s   (e) t = 800 s

Fig. 16. Temperature response of the hydrofrack simulation at various times corresponding to Fig. 15.

ture the effects of stress concentrations associated with the presence of the well bore in a biaxial stress state. The results of Figs. 8 and 9 do not include any damage. Therefore, they represent the elastic response only. In the elastic case, we found that when the principal stress with the maximum magnitude became tensile, the dominant mode shifted from mode II to mode I. Recall that stress intensities and energy release rates are determined with respect to an oriented crack (see Fig. 2). As stated earlier, we assume that a microcrack exists inside each finite element and that it is oriented in the most favorable direction for the maximum energy release rate as calculated by Eq. (18). While these results were generated by employing a uniform pore fluid pressure, they are indicative of the results in the case of borehole over pressurization. That is, with equal principal stresses, when the highest magnitude principal stress becomes tensile around the well bore, the mode changes to mode I and the mode II response drops to zero as seen in Fig. 9(b).

8.2.2. Equivalent principal stress cases with damage

Figs. 11–13 display the result of simulations with the same 70 MPa vertical and horizontal principal stresses as Figs. 8(b) and 9(b) only with damage included. The introduction of damage results in a reduction in stress (see Fig. 3) in the damaged areas due to softening. This results in a lower injection pressure requirement to transition from mode II to mode I. In the elastic case of Figs. 8 and 9, the transition from mode II to mode I occurred at a

pore fluid pressure between 60 and 70 MPa. However, with damage included, the transition occurs at an injection pressure between 45 and 55 MPa. This indicates that the failure mode is opening even below the minimum far field principal stress (70 MPa).

In the simulations performed in Figs. 11–13, the initial pore fluid pressure was taken to be 35 MPa (half of the *in situ* principal stresses). The left hand images in each figure display the result for a cold water injection scenario where 100 °C water was injected into an initially 200 °C domain. The well was pressurized to 45 MPa in the first time step and held constant for the remainder of the simulation. The simulations employed a time step size of 100 s and ran 12 time steps (1200 total seconds). The images display the end state of the simulation. Fig. 11 displays the temperature response (left) and the pressure response (right) of the cold-water injection simulations of Figs. 12 and 13.

Fig. 12 displays the mode II response around the injection well for (Fig. 12(a)) the cold water and (Fig. 12(b)) the isothermal injection scenarios of Fig. 11. For scale, the extent of the mode II influence in (Fig. 12(a)) roughly corresponds to the temperature front seen in Fig. 11 (left). So, the area that has cooled is subjected to a small shearing mode II stress intensity. However, the magnitude of that stress intensity is not large enough to create any damage for the given uniform medium. Fig. 13 displays the mode I stress intensity result for the same simulations. Notice that in the cold water injection case (Fig. 13(a)), some mode I opening is present
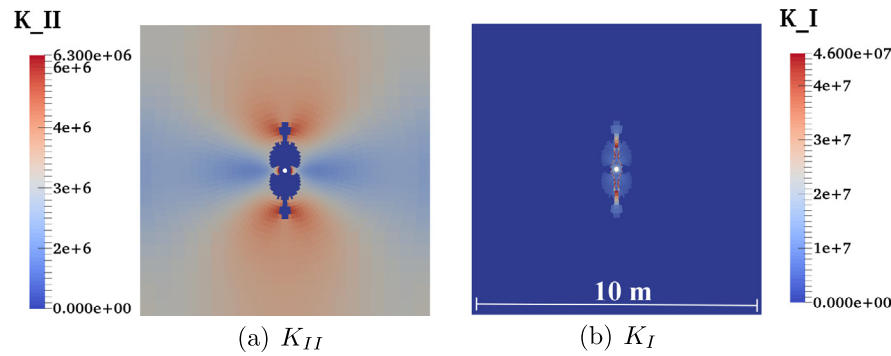
Fig. 17. The stress intensity responses for (a) mode II and (b) mode I for the hydrofrack simulation at 700 s.
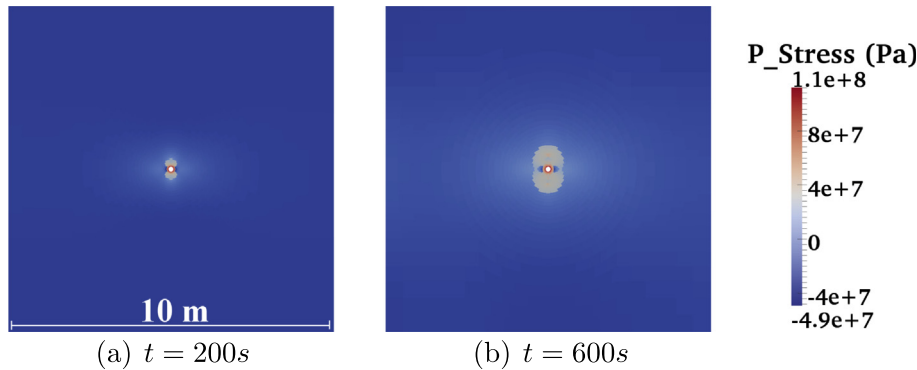

Fig. 18. The maximum principal stress result at 200 s (a) and 600 s (b) for the hydrofrack simulation.

at the well bore surface. This means that the reduction in temperature has reduced the stress state enough to transition from shear failure to opening failure near the well bore. However, in these simulations, the damage (Fig. 14) does not continue to propagate outward unless the injection pressure is further increased.

Fig. 14 displays the damage result for the simulations of Figs. 11–13. The damage is steady state in the images and would not continue to expand unless the injection pressure were increased or the injected fluid temperature were decreased. This is due to the choice of coefficient of thermal expansion β_s. A higher β_s value would result in larger displacements and a damage front following the cold water front. In this case, the pore fluid pressure alone is strong enough to cause damage, albeit mode II. However, the transition to mode I failure seen in Fig. 14(a) (the cold water injection scenario) resulted in more damage than in Fig. 14(b) the mode II controlled case (isothermal fluid injection). In summary, cold water injection has caused more damage than hot water injection, however that damage cannot propagate without a change in material parameters (β), an increase in well overpressure, or perhaps an existing weakness (fracture) in the area. This means that understanding *in situ* material parameters and fractures in the area of a stimulation well are very important to promoting controllable permeability enhancement.

8.2.3. Hydrofracking simulations with unequal principal stresses

Scenarios with equivalent horizontal and vertical principal stresses result in radial damage in the near well bore region (see Fig. 14). We sought to set up a biaxial stress state with unequal principal stresses in order to propagate a damage region similar to a crack. In this scenario, the horizontal principal stress was set to be $\sigma_H = 35$ MPa and the vertical principal stress was set to $\sigma_v = 70$ MPa. The initial pore fluid pressure was set to 20 MPa to be low enough to avoid mode I damage before any well bore

pressurization occurred. The well bore was pressurized to 110 MPa with 100 °C water. This situation most closely simulates a hydrofracking scenario. The injection pressure was much higher than previous simulations in this work because lower injection pressures resulted in small regions of localized damage near the well bore. A higher pressure scenario allowed for damage propagation analogous to crack propagation. Fig. 15 displays the damage at 100 s, 300 s, 500 s, 700 s, and 800 s after the onset of fluid injection. Notice that damage propagates nearly vertically – the expected direction given the stress state.

Fig. 16 displays the temperature response of the hydrofrack simulation at the same times reported in Fig. 15. The damaged zones result in an increase in permeability as calibrated in Section 8.1. The increase in permeability results in a greater cooling of the rock in and around those pathways due to the advected heat transfer. The rapid cooling of the rock and passing cold fluid from well to well is a scenario to avoid in geothermal energy extraction.

Fig. 17 displays the (Fig. 17(a)) mode II stress intensity and (Fig. 17(b)) mode I stress intensity responses at t = 700 s for the hydrofrack simulation. The areas far away from the well bore, that are subjected to a biaxial compressive stress state and are not affected by the damage zone near the well bore are predominately in a mode II regime. However, the areas of damage near the well bore are opening primarily in tension (mode I). Fig. 18 shows the maximum principal stress result of the cold water injection scenario at $t = 200$ s (Fig. 18(a)) and $t = 600$ s (Fig. 18(c)) after injection. The tensile stresses develop as a result of the high injection pressure in the area where mode I is dominant.

9. Conclusions and future work

Damage mechanics offers a natural framework for numerical THM modeling for the investigation of injection-induced damage

and permeability evolution in geothermal energy settings. In this work, we applied an energy release rate microcrack model in mixed modes (opening – I and shear – II) to simulate damage and permeability enhancement in confined compression tests and well bore injection scenarios of isothermal fluid and cold water injection. We calibrated the model with some basic stress–strain data for reservoir sandstones, but it is our immediate aim to calibrate the model with both confined and unconfined compression test data with Greywacke basement rock samples from New Zealand.

In a uniform medium (as tested here), it is obvious that fractures cannot propagate at low injection pressures. Injection pressures that are too low (even if mode I opening is present) result in damage areas being limited to very near the well bore. For engineered geothermal energy production, the aim is to enhance permeability in a large volume of rock. With a single injection well, with the stress state tested here, and a uniform medium, this is physically impossible. However, reservoir rock is not uniform as heterogeneity and anisotropy are the norm in the Earth's crust. The spatial distribution of *in situ* damage, permeability/porosity, and other material parameters is likely to play a key role in the ability to stimulate a large volume of rock at less than hydrofrack required pressurizations. Further, multi-well injection strategies need to be explored with this approach for the potential to stimulate a large volume of rock. The utility of this approach is that damage mechanics for solid mechanics constitutive theory is straightforward to implement in numerical finite element codes and offers a way to account for deformation induced damage. This approach offers a mixed-mode formulation that can account for both tensile and shear failures as both are of interest in the geothermal energy sector. This is an effect that has not been taken into account in previous THM simulations.

Acknowledgements

References

[1] Anderson T. Fracture mechanics: fundamentals and applications. 3rd ed. CRC Press, Taylor and Francis Group; 2005.

[2] Barenblatt G. The formation of equilibrium cracks during brittle fracture. general ideas and hypotheses. Axially-symmetric cracks. Appl Math Mech 1959;23:434–44.

[3] Besson J, Cailletaud G, Chaboche J. Nonlinear mechanics of materials (solid mechanics and its applications). Springer; 2010.

[4] Bonet J, Wood R. Nonlinear continuum mechanics for finite element analysis. Cambridge, UK: Cambridge University Press; 2008.

[5] Britto A, Gunn M. Critical state soil mechanics via finite elements. Chichester, UK: Ellis Horwood Limited; 1987.

[6] Carrier B, Granet S. Numerical modeling of hydraulic fracture problem in permeable medium using cohesive zone model. Eng Fract Mech 2012;79:312–28.

[7] Chen Z, Bunger A, Zhang X, Jeffery R. Cohesive zone finite element-based modeling of hydraulic fractures. Acta Mech Solids Sin 2009;22(5):443–52.

[8] Cladouhos T, Petty S, Iovenitti J, Levesay B, Baria R. Toward more efficient heat mining: a planned enhanced geothermal system demonstration project. In: Geoth Resources Council Trans. CA, USA: Davis; 2009.

[9] Clark J. A hydraulic process for increasing the productivity of wells. Trans Soc Petrol Eng AIME 1949;186:1–8.

[10] de Borst R, Crisfield M, Remmers J, Verhoosel C. Damage mechanics. In: Nonlinear finite element analysis of solids and structures. Chichester, England: John Wiley and Sons Ltd.; 2012.

[11] Dempsey D, Kelkar S, Lewis K, Hickman S, Davatzes N, Moos D, et al. Modeling shear stimulation of the desert peak egs well 27–15 using a coupled thermal–hydrological–mechanical simulator. In: Proceedings: 47th US rock mechanics/geomechanics symposium. San Francisco (CA), USA; 2013.

[12] Dugdale D. Yielding of steel sheets containing slits. J Mech Phys Solids 1960;8:100–4.

[13] Eftis J, Subramonian N. The inclined crack under biaxial load. Eng Fract Mech 1978:43–67.

[14] Gangi A. Variation of whole and fractured porous rock permeability with confining pressure. Int J Rock Mech Mineral Sci Geomech 1978:249–57.

[15] Griffith A. The phenomena of rupture and flow in solids. Philos Trans Ser A 1920:163–98.

[16] Gupta P, Duarte C. Simulation of non-planar three-dimensional hydraulic fracture propagation. Int J Numer Anal Meth Geomech 2014:1397–430.

[17] Halm D, Dragon A. A model of anisotropic damage by mesocrack growth: unilateral effect. Int J Damage Mech 1996:384–402.

[18] Hillerborg A, Modeer M, Petersson P. Analysis of crack formation and crack growth in concrete by means of fracture mechanics and finite elements. Cem Concr Res 1976;6:773–82.

[19] Ingebritsen S, Sanford W, Neuzil C. Groundwater in geologic processes. New York: Cambridge University Press; 2006.

[20] Inglis C. Stresses in a plate due to the presence of cracks and sharp corners. Trans Inst Naval Architects 1913:219–41.

[21] Irwin G. Onset of fast crack propagation in high strength steel and aluminum alloys. In: Proceedings: sagamore research conference; 1956. p. 289–305.

[22] Kachanov L. Time of the rupture process under creep conditions. TVZ Akad Nauk S.S.R. Otd Tech. Nauk 8; 1958.

[23] Kanney J, Miller C, Kelley C. Convergence of iterative split-operator approaches for approximating nonlinear transport problems. Adv Water Resour 2003;26:247–61.

[24] Kelkar S, Zyvoloski G, Hickman S, Davatzes N, Moos D. Modeling coupled thermal-hydrological-mechanical processes during shear stimulation of an EGS well. In: Proceedings: 37th workshop on geothermal reservoir engineering. stanford university. Stanford (CA), USA; 2012.

[25] Khoei A, Moallemi S, Haghighat E. Thermo-hydro-mechanical modeling of impermeable discontinuity in saturated porous media with X-FEM technique. Eng Fract Mech 2012:701–23.

[26] Lee H, Cho T. Hydraulic characteristics of rough fractures in linear flow under normal and shear load. Rock Mech Rock Eng 2002:299–318.

[27] Lemaitre J. How to use damage mechanics. Nucl Eng Des 1984:233–45.

[28] Lemaitre J. A course on damage mechanics. Berlin, New York: Springer; 1996.

[29] Lewis R, Schrefler B. The finite element method in the static and dynamic deformation and consolidation of porous media. Chichester, England: John Wiley and Sons Ltd.; 1998.

[30] Lu Y, Elsworth D, Wang L. Microcrack-based coupled damage and flow modeling of fracturing evolution in permeable brittle rock. Comput Geotech 2013:226–44.

[31] Mazars J, Pijauder-Cabot G. Continuum damage theory – application to concrete. J Eng Mech 1989;115(2):345–65.

[32] Moes N, Belytschko T. Extended finite element method for cohesive crack growth. Eng Fract Mech 2002:813–33.

[33] Moes N, Dolbow J, Belytschko T. A finite element method for crack growth without remeshing. Numer Methods Eng 1999:131–50.

[34] Mohammadnejad T, Khoei A. An extended finite element method for hydraulic fracture propagation in deformable porous media with the cohesive crack model. Finite Elem Anal Des 2013:77–95.

[35] Nathenson M. The dependence of permeability on effective stress from flow tests at hot dry rock reservoirs in Rosemanowes (Cornwall) and Fenton Hill (New Mexico). Geothermics 1999:315–40.

[36] Pogacnik J, Leary P, Malin P. Physical/computational framework for EGS *in situ* fracture stimulation. In: Proceedings: New Zealand geothermal workshop. Auckland, New Zealand; 2012.

[37] Pogacnik J, O'Sullivan M, O'Sullivan J. A damage mechanics approach to modeling permeability enhancement in thermo-hydro-mechanical simulations. In: Proceedings: 39th workshop on geothermal reservoir engineering. Stanford University, Stanford (CA), USA; 2014.

[38] Pogacnik J, Podgorney R, Leary P. Computational EGS: modeling fully-coupled heat and fluid flow through a deformable fracture-permeable medium with the finite element method. In: Proceedings: 2012 conference of the engineering mechanics institute. June 17–20, 2012, Notre Dame (IN), USA; 2012.

[39] Rutqvist J, Dobson P, Garcia J, Oldenburg C, Vasco D, Walters M, et al. Pre-stimulation coupled THM modeling related to the northwest geysers EGS demonstration project. In: Proceedings: 38th workshop on geothermal reservoir engineering. Stanford University, Stanford (CA), USA; 2013.

[40] Sarris E, Papanastasiou P. The influence of the cohesive process zone in hydraulic fracture modelling. Int J Fract 2011:33–45.

[41] Tang C, Tham L, Lee P. Coupled analysis of flow, stress, and damage (FSD) in rock failure. Int J Rock Mech Min Sci 2002:477–89.

[42] Voyiadjis G, Kattan P. Damage mechanics. Boca Raton (FL), USA: CRC Press; 2005.

[43] Wang J, Park H. Fluid permeability of sedimentary rocks in a complete stress–strain process. Eng Geol 2002:291–300.

[44] Witherspoon P, Wang J, Iwai K, Gale J. Validity of cubic law for fluid flow in a deformable rock fracture. Water Resour Res 1980:1016–24.

[45] Yeh G, Tripathi V. Critical-evaluation of recent developments in hydrogeochemical transport models of reactive multichemical components. Water Resour Res 1989;25(1):93–108.

[46] Zhang R, Jiang Z, Sun Q, Zhu S. The relationship between the deformation mechanism and permeability of brittle rock. Nat Hazards 2013:1179–87.

[47] Zhou F, Molinari J. Dynamic crack propagation with cohesive elements: a methodology to address mesh dependency. Int J Numer Meth Eng 2004;59:1–24.

[48] Zhou J, Shao J, Xu W. Coupled modeling of damage growth and permeability variation in brittle rocks. Mech Res Commun 2006:450–9.